Chemical Science

ROYAL SOCIETY OF CHEMISTRY

EDGE ARTICLE

View Article Online
View Journal | View Issue

Cite this: *Chem. Sci.*, 2025, **16**, 20344

All publication charges for this article have been paid for by the Royal Society of Chemistry

Received 29th July 2025
Accepted 28th September 2025

DOI: 10.1039/d5sc05696a

rsc.li/chemical-science

Antimicrobial and breathable membranes with printed carbon nanotube-silver composite conductive layers for electronic sensing

Huacui Xiang,[a] Daniel Verrico,[c] Taher Hafiz,[c] Enjian He,[a] Gary E. Wnek,[c] Kun Hu,[d] Guojun Liu,*[b] Yen Wei *[a] and Jiujiang Ji*[ac]

With the accelerating advancement of wearable electronics, electronic skin (e-skin) has emerged as a promising technology for applications in health monitoring, prosthetics, and human–machine interfaces. Nonetheless, achieving simultaneous breathability, antibacterial properties, and high sensing fidelity presents a formidable challenge. In this study, we report a multifunctional electronic skin (e-skin) constructed from a modified Tecoflex (thermoplastic polyether-based polyurethane) electrospun nanofiber membrane (T-eNFM), integrating breathability, antibacterial activity, and high-fidelity sensing capabilities. The T-eNFM substrate promotes wearer comfort *via* its innate breathability while simultaneously inhibiting bacterial colonization through robust antimicrobial functionality. A composite of multi-walled carbon nanotubes (MWCNTs) and silver paste (Ag powder) was printed onto T-eNFM-3 to form a conductive, mechanically compliant sensing layer. The fabricated strain sensor exhibited a gauge factor of 5.81, while the multilayer pressure sensor displayed a sensitivity of 2.83 kPa^{-1}, rendering it ideally suited for monitoring cardiovascular physiological signals. This work outlines a blueprint for next-generation electronic skin devices by addressing the critical challenges of comfort, safety and multifunctionality.

Introduction

Electronic skin (e-skin) mimics the sensory functions of human skin and has attracted considerable attention for its promise in wearable healthcare, human–machine interaction and soft robotics.[1–3] By integrating flexible substrates with multimodal sensors, e-skin enables real-time monitoring of physiological signals, tactile feedback and environmental cues, thereby significantly expanding the capabilities of next-generation intelligent devices.[4,5] However, the sensitivity and long-term operational stability of pressure and strain sensors integrated on polyimide (PI) or polydimethylsiloxane (PDMS) flexible substrates remain significantly constrained. Conventional electronic skin platforms frequently face a trade-off between sensitivity and user comfort, underscoring an urgent demand for design strategies that reconcile high-performance sensing with wearability.[6,7] Moreover, most electronic skin materials are engineered to maximize sensing performance, often at the expense of essential attributes such as antibacterial activity and breathability.[8,9] In skin-contact deployments, insufficient air permeability and unchecked microbial colonization can compromise both comfort and safety.[10–12] For example, during prolonged health-monitoring, sweat and bacteria trapped against a non-breathable e-skin interface may provoke skin irritation or infection, thereby undermining the reliability of continuous measurements.[13,14] Addressing these shortcomings requires the design of e-skins that seamlessly integrate antibacterial efficacy, enhanced breathability and robust, high-fidelity sensing within a single, cohesive architecture.[15,16]

Electrospun nanofibrous membranes (eNFM), characterized by their high surface area, tunable porosity, flexibility, and ability to conform to complex curved surfaces, provide a versatile platform for applications in wearable sensors.[17–19] Their nanoscale fiber diameters, interconnected pore networks and modifiable surface chemistry have drawn intense interest in the field of wearable, flexible sensing.[20,21] However, the emergence of antimicrobial resistance has impeded the translation of eNFM into practical applications.[22,23] Owing to their entangled micro/nanofibers, eNFM form highly porous three-dimensional networks with exceptional pore interconnectivity, making them ideal substrates for cell adhesion and proliferation.[22] Simultaneously, the relentless emergence of drug-resistant bacteria has driven growing interest in endowing eNFM with intrinsic

[a]*The Key Laboratory of Bioorganic Phosphorus Chemistry & Chemical Biology, Department of Chemistry, Tsinghua University, Beijing, 100084, China. E-mail: weiyen@tsinghua.edu.cn*

[b]*Suzhou Institute for Advanced Research, University of Science and Technology of China, Suzhou 215123, China. E-mail: liuguojun@ustc.edu.cn*

[c]*Macromolecular Science and Engineering, Case Western Reserve University, Cleveland, OH 44106, USA. E-mail: jjj.2021@tsinghua.org.cn*

[d]*School of Printing and Packaging Engineering, Beijing Institute of Graphic Communication, Beijing 102600, China*

bactericidal properties, thereby obviating the need for antibiotic incorporation.[24,25] Tecoflex is a thermoplastic polyurethane synthesized from methylenebis(cyclohexyl) diisocyanate, poly (tetramethylethylene glycol), and 1,4-butanediol, and is distinguished by its exceptional flexibility and processability. Electrospun Tecoflex EG-80A yields a highly flexible fabric that serves as a promising substrate for wearable device applications.[26,27] However, driven by the demand for safer, more conformable materials, researchers are now focusing on integrating antibacterial functionality into skin-conformable electronics to prevent device fouling and mitigate infection risks during biomedical monitoring.[28,29] The incorporation of antibacterial functionalities into skin-conformable electronic devices has emerged as a key strategy to prevent device contamination and mitigate infection risk. Accordingly, embedding antibacterial agents—including metallic nanoparticles (Ag, Au), metal-oxide (ZnO, CuO, TiO_2) and metal-sulfide nanoparticles, and carbon-based nanomaterials—directly within fiber matrices, or grafting quaternary ammonium compounds, biguanides, and pyridine derivatives onto fiber surfaces, represents a highly promising strategies for infection control in both biomedical and environmental applications.[30–34] Concurrently, the safe and efficient incorporation of fungicides into eNFM to bolster the antifungal performance of electronic sensors represents a critical frontier in safeguarding human health.[35,36]

In this work, we report a multifunctional electronic skin (e-skin) based on a modified Tecoflex electrospun nanofiber membrane (T-eNFM) that synergistically integrates intrinsic breathability with potent antibacterial activity, ensuring wearer

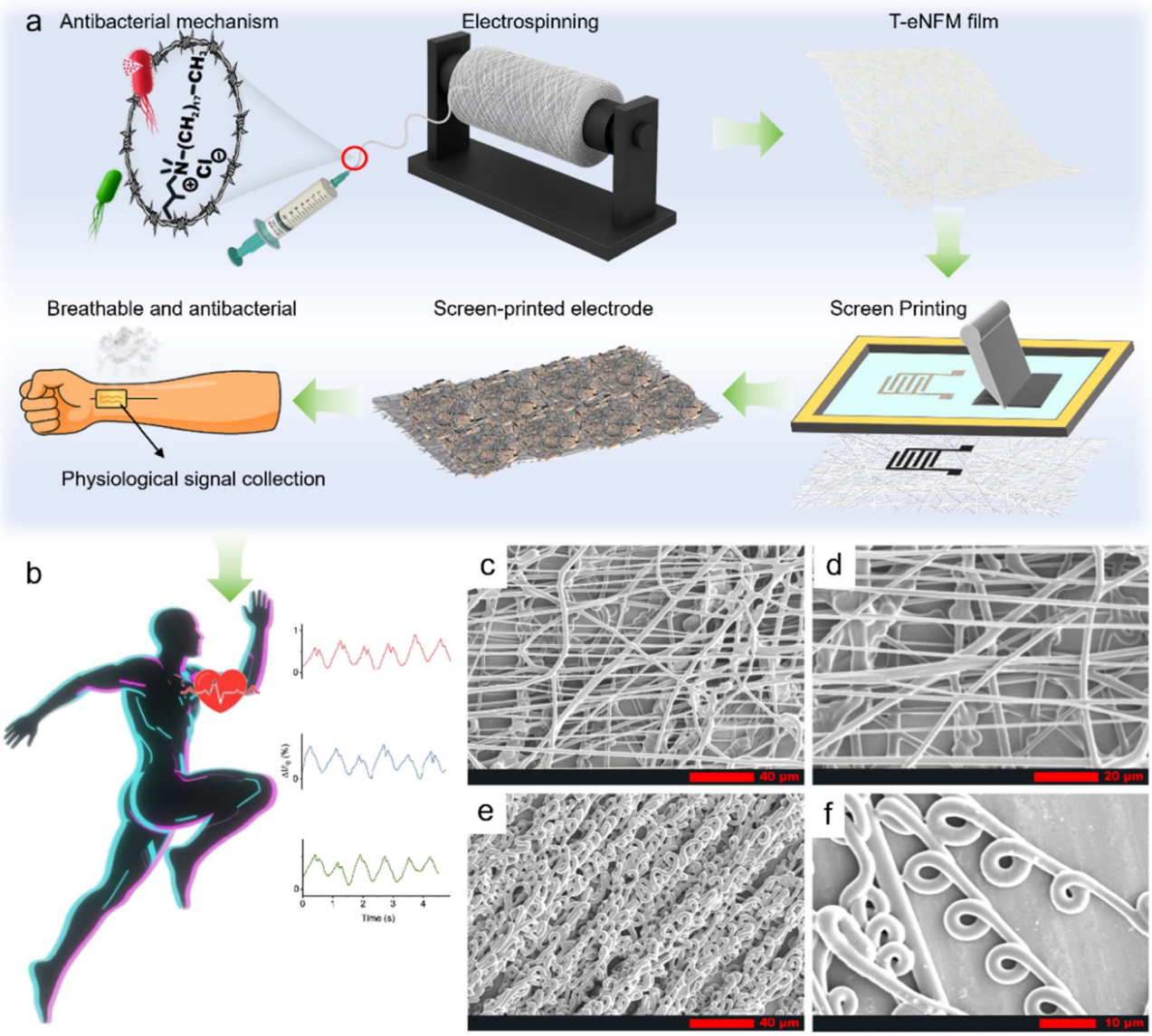

Fig. 1 (a) Design and preparation of antibacterial and breathable electronic skin. (b) Electronic skin can be applied to human body sensing and for detecting physiological signals of the cardiovascular system. SEM images of the (c and d) fiber structures of T-eNFM-0 and (e and f) the regular spiral fiber structure presented by T-eNFM-3 at different magnifications.

comfort and effective inhibition of bacterial colonization. A composite ink of multi-walled carbon nanotubes (MWCNTs) and silver paste (Ag powder) was printed onto the T-eNFM-3 to yield an e-skin with exceptional electrical conductivity and mechanical compliance. The engineered wearable electronic skin (e-skin) features sensitive and stable pressure and strain sensors, enabling detection of human motion and monitoring of cardiovascular physiological signals *via* its micro-structured sensitive layer. By seamlessly integrating antibacterial functionality, breathability, and high-performance sensing within a unified structure, this e-skin design addresses limitations of conventional platforms and establishes a foundation for robust, translational applications.

Results and discussion

Antimicrobial and breathable electronic skin

To address the issues of insufficient antibacterial performance and poor breathability of current electronic skin, a new type of electronic skin with antibacterial, breathable and excellent sensing performance was developed. The synthesis procedures and characterizations of the (2,3-dihydroxypropyl)-*N*,*N*-dimethyloctadecan-1-aminium chloride (DOQA) and modified Tecoflex polymer were listed in the Supplementary Information (Fig. S1–S3). The Tecoflex membrane with antibacterial and breathable properties was prepared by electrospinning, while surface-microstructured electrodes were formed using screen printing (Fig. 1a). Strain and pressure sensing modalities were integrated to realize an electronic skin capable of detecting human motion and monitoring cardiovascular physiological signals (Fig. 1b). T-eNFM-3 exhibited superior stretchability and toughness, attributed to its helical fiber architecture, which significantly broadens its elastic range compared with other T-eNFM materials. This phenomenon may be attributed to the incorporation of DOQA, which modifies the molecular interactions within Tecoflex, thereby generating contraction forces that lead to the formation of helical fiber structures. The surface morphology of T-eNFM was observed by SEM. As shown in Fig. 1c and d, T-eNFM-0 presents a simple fiber structure, while T-eNFM-3 presents a regular helical fiber structure (Fig. 1e and f). The SEM of other samples can be found in Fig. S4.

To enable sensing functionality, a composite of multi-walled carbon nanotubes (MWCNTs) and silver paste (Ag powder) was deposited onto the T-eNFM surface *via* screen printing to form a conductive layer. As shown in Fig. 2a, conductive ink of optimized viscosity was screen-printed onto the T-eNFM surface. The microstructure of the resulting conductive layer was characterized *via* scanning electron microscopy (SEM). The MWCNTs and Ag paste were stacked and interlaced with each other to form a dense conductive layer. To prepare a conductive layer with a microstructure, as shown in Fig. 2b, the viscosity of the screen-printed ink was adjusted by the content of thickener carboxymethyl cellulose (CMC), and a microstructure was formed on the printed conductive layer. Upon separation from the screen, the high-viscosity ink exhibited reduced surface tension that inhibited capillary-driven smoothing, yielding

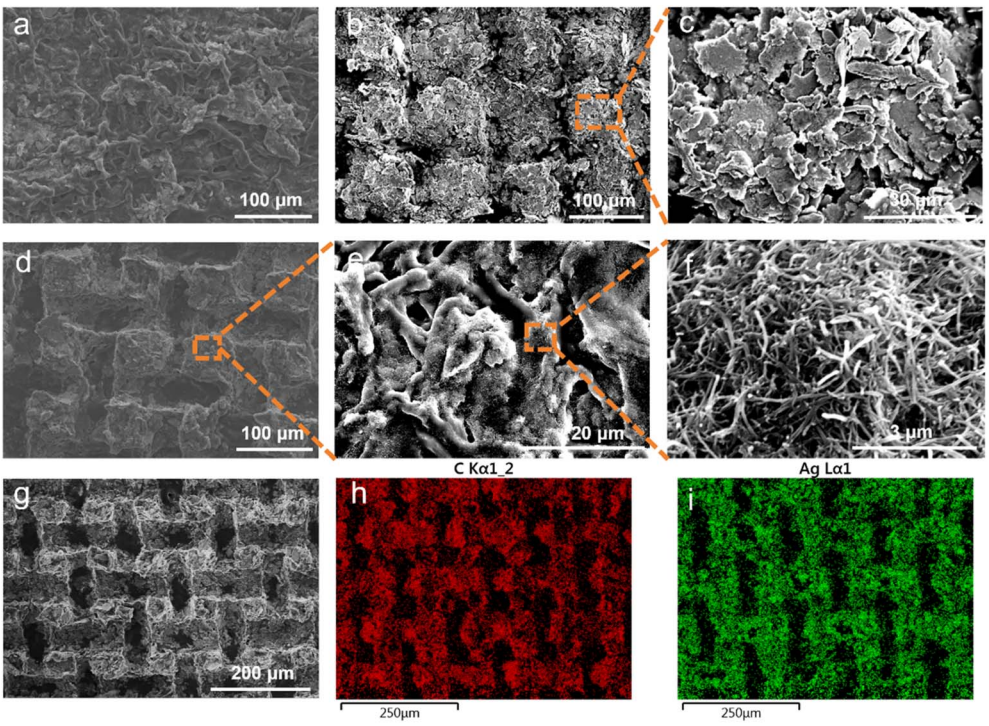

Fig. 2 The surface morphology of the T-eNFM printed electrode. (a) T-eNFM surface screen-printed conductive layer. (b) Microstructure conductive layer of Ag paste printed on T-eNFM surface by screen printing and (c) its local magnified image. (d) Microstructure conductive layer of MWCNTs and Ag paste printed on T-eNFM surface by screen printing and (e and f) local magnified image. (g) The surface screen printing of T-eNFM features a regular array of microstructure conductive layers and the distribution of (h) C element in the MWCNTs and (i) Ag element.

persistent net-hole imprints and an array of microscopic protrusions across its surface. Screen-printed Ag electrodes revealed stacked silver flakes forming layered architectures (Fig. 2b and c). Upon incorporation of CMC into the conductive ink and subsequent screen printing (Fig. 2d), a grid-like microarchitecture emerges, characterized by interlocking nanotubes and silver flakes that coalesce into a densely packed conductive network (Fig. 2e and f). Energy-dispersive X-ray spectroscopy (EDS) revealed a uniform dispersion of carbon and silver across the electrode surface, with pronounced stacking within the microstructured domains (Fig. 2g). Elemental mapping of carbon (Fig. 2h) and silver (Fig. 2i) further confirmed the homogeneous distribution and structural integrity of the printed conductive layer.

Performance characterization of T-eNFM materials

The surface properties of the material were characterized by Fourier-Transform Infrared (FTIR) and X-ray photoelectron spectrometer (XPS) as shown in Fig. S5 and 3a. The characteristic peaks that occurred within the range of 2948–2850 cm^{-1} were attributed to the stretching vibrations of $-CH_3$ and $-CH_2$. The characteristic peaks that appeared near 1460 cm^{-1} and 1471 cm^{-1} were the bending vibration peaks of $-CH_3$ and $-CH_2$

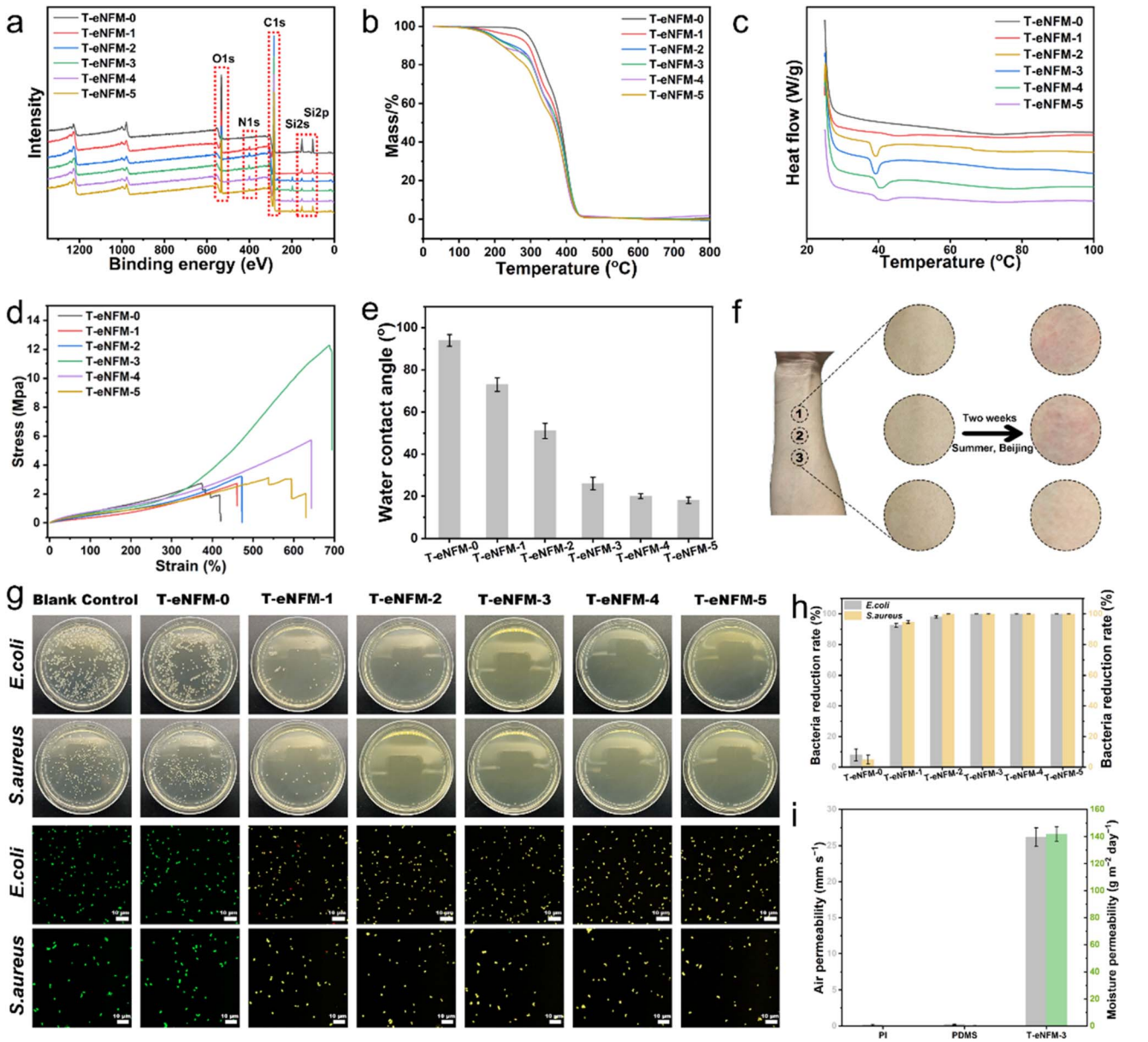

Fig. 3 (a–c) The XPS, TGA, and DSC of T-eNFM materials. (d) Stress–strain curves of T-eNFM materials. (e) The water contact angles on surfaces of block T-eNFM. (f) Skin irritation observed on the forearm of volunteer ((1) polyimide (PI); (2) polydimethylsiloxane (PDMS); (3) T-eNFM-3). (g) Digital images of antibacterial performance on surfaces of blank control and block T-eNFM materials incubated with *E. coli* and *S. aureus* for 12 h; images of live/dead fluorescence assays of *E. coli* and *S. aureus* adhered to different T-eNFM block material surfaces. (h) Bacteria reduction rate of different T-eNFM materials. (i) The air and moisture permeability properties of different materials.

respectively. Additionally, a stretching vibration peak of C–N was observed near 1040 cm^{-1} on the FTIR spectrum, indicating the success of the quaternization reaction. As indicated in Table S1, the atomic content of N 1s increased from 0.29% in T-eNFM-0 to 2.25% in T-eNFM-5, confirming the uniform distribution of the modified Tecoflex and highlighting the efficiency of DOQA as a surface functionalization agent.

The thermogravimetric analysis (TGA) was used to measure the thermal stability of T-eNFM materials. As shown in Fig. 3b, all samples undergo two distinct stages of thermal degradation. The initial stage corresponds to the decomposition of the hard segments in Tecoflex, followed by further degradation of the macromolecular structure within the soft segments. The onset decomposition temperature ($T_{5\%}$), defined as the temperature at which 5% weight loss occurs, serves as a critical indicator of polymer thermal stability. Notably, the $T_{5\%}$ decreases progressively with increasing DOQA content, suggesting that DOQA incorporation compromises the thermal stability of Tecoflex. This reduction likely arises from the weaker thermal stability of bonds formed between Tecoflex and the hydroxyl groups at the DOQA termini compared to Tecoflex's intrinsic bonding. This may also contribute to the development of helical morphology in T-eNFM-3 spun fibers. The incorporation of DOQA modulates the internal molecular interactions within Tecoflex, generating contraction forces that ultimately result in the helical configuration of the fabricated fibers. Furthermore, the differential scanning calorimeter (DSC) curve was depicted in Fig. 3c. The melting temperature (T_m) of the hard segments reflects the degree of aggregation inside the modified Tecoflex. As the DOQA mass fraction increased, the T_m rose from 38.88 °C to 41.95 °C, indicating that DOQA disrupts the ordered aggregation of hard segments in Tecoflex and generates more loosely packed hard domains. These less ordered domains enhance chain mobility in the hard-segment phase and thereby amplify the overall phase separation of Tecoflex. Furthermore, the stress–strain behavior of various T-eNFM materials was evaluated in Fig. 3d. T-eNFM-3 demonstrated a tensile strength of 12.25 MPa and an elongation at break of 680%, marking a 1.84-fold improvement in tensile strength compared to T-eNFM-0 (370%). Owing to the uniform helical architecture of the T-eNFM-3 mat, stress–strain were measured both along and perpendicular to the helical structure as shown in Fig. S6. The helical architecture of the T-eNFM-3 mat significantly enhances its tensile performance, thereby substantially widening its elastic range compared with other samples. However, as the DOQA content increases, the tensile strength of the material declines due to the disruption of the helical fiber structure generated during electrospinning. Notably, the fiber structure of T-eNFM-5 extends to several hundred micrometers, substantially compromising its mechanical integrity (Fig. S4). As shown in Fig. S7, the correlation between spinning parameters and helical structure of T-eNFM-5 was further examined. The helical structure of T-eNFM-3 is highly sensitive to spinning temperature: increasing the temperature enhances the fluidity of the spinning solution, which in turn disrupts the fiber's helical configuration. Additionally, the rotational speed of the fiber collector directly influenced spinning uniformity; speeds above 350 rpm leaded to a noticeable deterioration in fiber uniformity.

The hydrophilicity and hydrophobicity of electrospun fiber membranes play a critical role in determining wearing comfort. As depicted in Fig. 3e, the hydrophilicity of T-eNFM increases with rising DOQA content, decreasing the water contact angle from 94 ± 2.8° (T-eNFM-0) to 18 ± 1.5° (T-eNFM-5). This improvement is attributed to the strong affinity of quaternary ammonium cations for water molecules. Enhanced hydrophilicity is anticipated to promote wearing comfort in flexible wearable electronics. Additionally, the breathability and moisture permeability of the base material used in wearable devices are critical factors influencing user comfort and dermatological health. Prolonged adhesion of a substrate to skin can induce thermophysiological discomforts such as dampness, desiccation and inflammation. Consequently, besides exceptional sensing performance, electronic skin (e-skin) demands a highly breathable substrate (Fig. 3f). Compared with polyimide (PI) and polydimethylsiloxane (PDMS) films, T-eNFM-3 demonstrated an air permeability of 26.2 ± 1.3 mm s^{-1} and a moisture vapor transmission rate of 142.1 ± 5.2 g m^{-2} day^{-1}, markedly surpassing those of conventional flexible films used in wearable electronics (Fig. 3i).

As shown in Fig. 3g, the inhibition rate of colony-forming units (CFUs) on agar plates was employed to evaluate the antibacterial efficacy of the coating surface. Relative to the blank control, antibacterial activity of the T-eNFM surfaces increased with higher DOQA content. The surfaces of T-eNFM-3, T-eNFM-4 and T-eNFM-5 exhibited antibacterial rates up to 99.9% against *E. coli* and *S. aureus* (Fig. 3h). To further assess the antibacterial activity of the coatings, SYTO 9/propidium iodide staining was performed to evaluate the viability of *Escherichia coli* and *Staphylococcus aureus* recovered from the coating surfaces. On T-eNFM-3, T-eNFM-4 and T-eNFM-5, nearly all cells were co-stained with SYTO 9 (live/dead) and PI (dead), indicating that incorporation of DOQA confers potent bactericidal properties.

Strain and pressure sensing performance

The viscosity of the ink was adjusted using CMC, and a conductive layer with microstructures was formed on the surface of T-eNFM-3 through screen printing. As illustrated in Fig. 4a, the printing ink exhibited excessive fluidity in the absence of CMC, impeding effective deposition. Addition of 1 wt% CMC conferred a suitable viscosity of 1420 mPa s, permitting uniform printing onto the T-eNFM-3 substrate and yielding a planar conductive layer. With further increases in CMC content, the ink viscosity rose progressively. At 2 wt% CMC, a composite ink comprising the thickening agent, MWCNTs, and silver was successfully deposited onto T-eNFM-3 *via* screen printing. Following separation of the ink from the screen plate, its elevated viscosity led to a reduction in surface tension, hindering rapid self-leveling and the erasure of mesh imprint traces. Consequently, regularly patterned raised microstructures emerged on the surface of T-eNFM-3. Nevertheless, additional increases in CMC content caused the ink

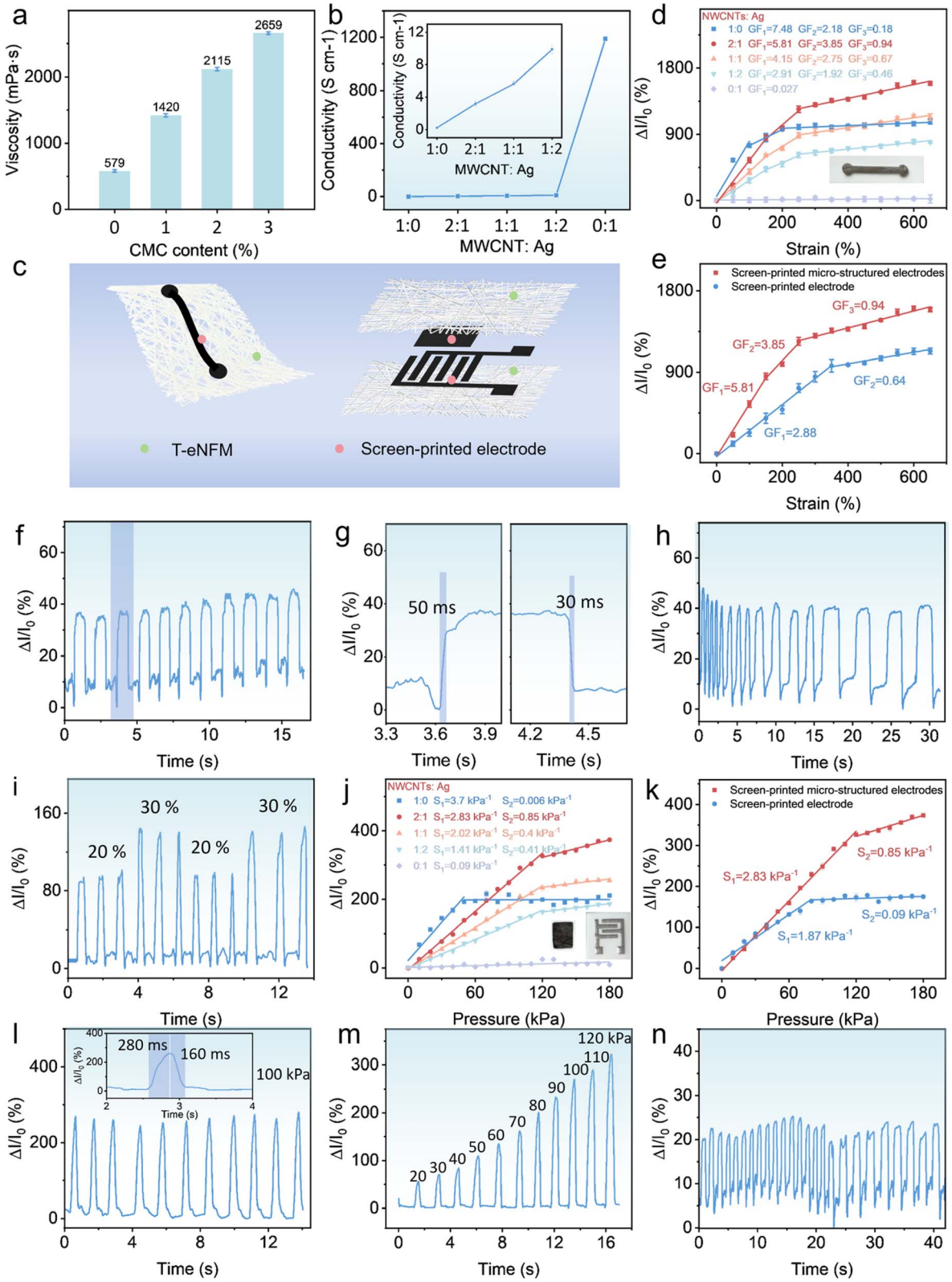

Fig. 4 (a) Viscosity of the MWCNTs and Ag paste mixed ink. (b) The conductivity of the electrodes fabricated by screen printing with ink mixtures of MWCNTs and Ag paste in different proportions. (c) Structural diagrams of the strain sensor and pressure sensor. (d) Sensing sensitivity of strain sensors formed by different proportions of MWCNTs and Ag paste. (e) The sensitivity of strain sensors with microstructure and those without microstructure. (f) The sensing signals of the strain sensor under cyclic strain conditions and (g) response time. (h) The strain sensor can provide stable sensing signals under different frequencies and (i) different strains during the cyclic process. (j) Sensing sensitivity of pressure sensors formed by different proportions of MWCNTs and Ag paste. (k) The sensitivity of pressure sensors with microstructures and those without microstructures. (l) The stable electrical signals and response time of the pressure sensor during the cycle. (m) The pressure sensor generates sensing signals under different pressures and (n) at different frequencies.

viscosity to exceed optimal levels, resulting in screen plate clogging and precluding effective deposition. The ratio of MWCNTs to Ag paste in the screen-printing ink plays a critical role in modulating the electrical conductivity and sensing performance of the electrodes. Therefore, we chose to print the micro-structured conductive layer using an ink with 2% CMC added. Accordingly, five ink formulations with MWCNTs : Ag paste mass ratios of 1 : 0, 2 : 1, 1 : 1, 1 : 2, and 0 : 1 were prepared, as depicted in Fig. 4b. The conductivity of the screen-printed pure MWCNTs and Ag paste electrodes was 0.223 S cm^{-1} and 1190 S cm^{-1} respectively, and the conductivity of the screen-printed mixed electrodes of MWCNTs and Ag paste gradually increased with the increase in Ag content. The addition of Ag part effectively enhances the electrical conductivity of the conductive layer. The printed strip-shaped conductive electrodes were used for strain detection, and the printed square electrodes were combined with Ag finger-type electrodes to form a pressure sensor (Fig. 4c).

The conductive layers prepared by printing different proportions of MWCNTs and Ag inks were used to fabricate sensors, and their sensing performances were investigated. As shown in Fig. 4d, the strain sensor is fabricated by screen printing. The strain sensor made of pure Ag paste has very low sensitivity. Ag is a highly conductive metal, but the silver sheet layer is relatively rigid and has poor flexibility. On the flexible antibacterial breathable membrane substrate, the silver conductive layer is dense and stable, but when subjected to strain, it is prone to cause the separation of the membrane due to the deformation of the substrate, resulting in a sudden interruption of the conductive path and unstable resistance change, thus causing the sensor to have low sensitivity (GF = 2.36) and poor repeatability. With the addition of MWCNTs, these nanotubes serve as a flexible framework that bridges dispersed silver sheets by leveraging their high aspect ratio. This forms a continuous network of silver sheets and MWCNTs, enabling synchronous deformation with the substrate and allowing fine-tuning of the conductive layer's electrical properties. At the same time, the presence of a certain amount of silver sheets can enhance the structural strength of the electrode, avoiding irreversible fractures of the MWCNTs network due to excessive deformation. When the ratio of MWCNTs to Ag paste is 1 : 2 and 1 : 1, the sensor exhibits different sensing sensitivities within different strain ranges of 0–150%, 150–250%, and 250–650%. As the content of MWCNTs increases, the sensor's sensitivity also increases. When the content of MWCNTs further increases to 2 : 1, the content of MWCNTs is sufficient to support the framework, and the content of the Ag is moderate, not prone to agglomeration. In the conductive path, three contact forms, "Ag – Ag", "Ag – MWCNTs", and "MWCNTs – MWCNTs", coexist. Under the action of strain, the distance changes and contact area changes at the contact points are more significant, resulting in a greater change in the resistance rate of the sensor and higher sensitivity. The sensor has GF = 5.81, 3.85, and 0.94 in the strain ranges of 0–150%, 150–250%, and 250–650%, respectively. Pure MWCNTs sensors have excellent flexibility and aspect ratio, and are easy to form into a network structure, but their conductivity is much lower than silver. In the pure MWCNTs network, the main conductive paths between tubes mainly rely on point contact, and the contact resistance is relatively high; moreover, a high proportion of MWCNTs may cause the network to be too dense due to agglomeration, resulting in a smaller change in the path during deformation, and the resistance changes rapidly at small strains (0–100%) but quickly reaches the limit, resulting in a smaller sensing range. When there is a large strain, the resistance change rate is low, and the sensitivity is insufficient. It was also verified that the micro-structured strain sensor by screen printing exhibited significantly enhanced sensing performance compared to the sensor without microstructure (Fig. 4e). In the case of the unstructured sensor, during repeated stretching deformation, the sensitive material is prone to crack or fall off due to stress concentration, especially at the interface with the substrate, resulting in rapid performance degradation. The porous microstructure can buffer the stress, disperse it, and reduce the generation of cracks within the material, enabling the sensor to maintain stable performance after cycling while maintaining high flexibility (able to adapt to complex curved surfaces, such as human skin and robot joints).

Further tests were conducted on the sensing performance of the strain sensor, as shown in Fig. 4f. Under a 10% cyclic strain condition, the strain sensor exhibited a stable and repetitive current signal. One of the cycles in Fig. 4f was enlarged to obtain Fig. 5g. The response time and recovery time of the sensor were 50 ms and 30 ms respectively. Additionally, this strain sensor can detect stable repetitive sensing signals under different frequencies of strain cycles (Fig. 4h). When applying different strains to the sensor, as shown in Fig. 4i, the sensor still showed stable sensing signals during the cyclic changes of 20% and 30% strain. These indicate that the fabricated strain sensors possess stable and reliable sensing performance. The long-term stability of the sensor is an important factor. To verify whether the strain sensor can be used stably for a long time, we conducted 10 000 strain cycling tests on the prepared strain sensor (Fig. S8a–c). The test results showed that the strain sensor exhibited excellent stability. After repeating the strain application, the current change rate did not show significant attenuation, indicating that this sensor has reliable stability.

A multi-layer structure pressure sensor was constructed by using printed Ag paste finger-type electrodes and a MWCNTs/Ag paste composite conductive electrode. As shown in Fig. 4j, when the electrodes are pure Ag paste, due to the rigid collision between the Ag, the conductive path is easily saturated quickly. This pressure sensor has low sensitivity. The initial resistance of pure Ag paste is very low. Even if ΔR changes due to pressure, the sensitivity may still be low; moreover, when the Ag part is in the dominant contact state, the path changes are mostly step-like transitions between open and closed, resulting in poor response linearity. When MWCNTs are added and the sensor is under pressure deformation, the contact area between the Ag part and MWCNTs increases, and the resistance decreases. After removing the pressure, the elastic recovery force of MWCNTs causes the contact area to decrease, resulting in an increase in resistance. This "compression – recovery" reversibility is more significant at a 2 : 1 ratio. The sensor has

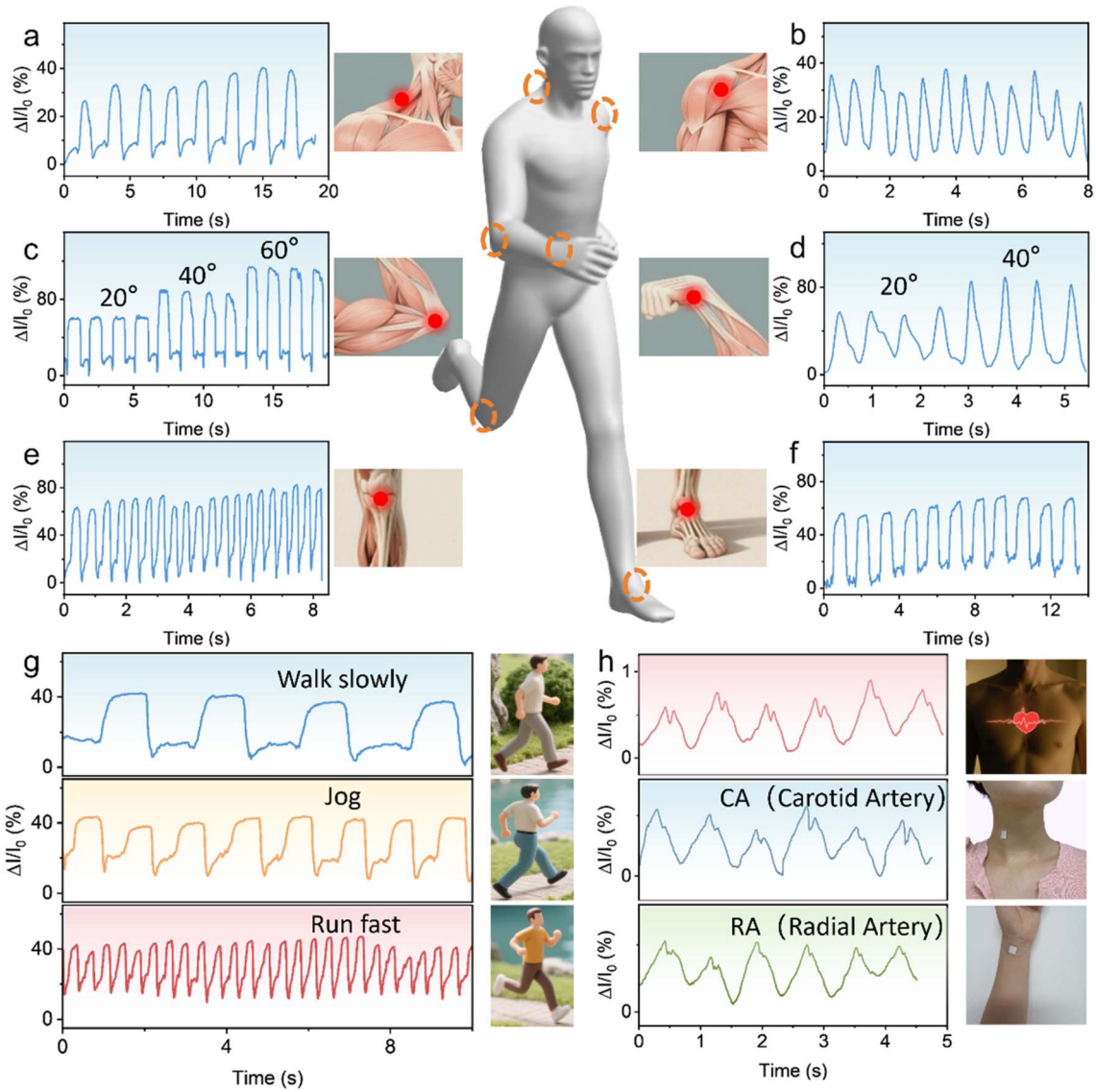

Fig. 5 The strain sensors continuously monitor the (a) neck, (b) shoulders, and (c) elbows at different degrees of flexion, (d) wrists, (e) knees, and (f) ankles of the body during movement. (g) The strain sensors monitor slow walking, jogging and sprinting in real time. (h) The pressure sensors monitor the heartbeats, carotid arteries and radial arteries in real time.

a sensitivity $S = 2.83\ \text{kPa}^{-1}$ in the pressure range of 0–120 kPa and $0.85\ \text{kPa}^{-1}$ in the range of 120–180 kPa. The silver sheet provides rigid support, and MWCNTs provide elastic recovery. The initial resistance of the pure MWCNTs pressure sensor is high, and the network is dense. The contact points quickly reach saturation within a small pressure range of 0–50 kPa. As the pressure increases, the amplitude change of ΔI is small, resulting in low sensitivity. In addition, compared to the pressure sensor composed of Ag and finger electrodes, the microstructured electrodes by screen printing have significantly improved sensing performance compared to the pressure sensor without microstructure (Fig. 4k). For the MWCNTs and Ag paste composite electrodes, the amplification of local deformation directly leads to more drastic changes in the conductive path at the contact points of MWCNTs and Ag paste, resulting in a significant increase in the rate of current change and thus an improvement in sensitivity. In the planar structure of screen printing, the contact points between the MWCNTs and Ag part are evenly distributed but have a lower density, with most being large-area bonded strong contact points. When subjected to external force, only a few contact points separate or approach, and the resistance change range is relatively small.

Further verification of the sensing performance of the pressure sensor. Fig. 4l shows the stable electrical signal generated by the pressure sensor during the 100 kPa pressure cycle. Meanwhile, the local magnified Fig. 4l indicates that the response time of the pressure sensor is 280 ms and the recovery time is 160 ms. At the same time, the pressure sensor exhibits stable and reliable current signals under different pressures ranging from 20 to 120 kPa (Fig. 4m). Additionally, the pressure

sensor also generates stable and cyclic sensing signals at different frequencies (Fig. 4n). These data confirm that the pressure sensor composed of the micro-structured electrodes printed by screen printing has reliable and stable sensing performance. The long-term stability of the pressure sensor was further verified. As shown in Fig. S8d–f, the pressure sensor was subjected to 10 000 pressure cycle tests. The test results still demonstrated excellent stability, and the current change rate did not show any significant attenuation, indicating that this pressure sensor has long-term stability.

Application demonstrations

Due to the excellent breathability, antibacterial properties and high elasticity of T-eNFM-3, the sensor constructed by screen printing micro-structured electrodes on the surface of T-eNFM-3 can be used in electronic skin. The strain sensor, which is attached to the surface of the skin, can detect the deformation of different parts of the human body (such as the neck, shoulders, elbows, wrists, knees and ankles) during movement in real time (Fig. 5a–f), to track the deformation caused by joint bending and convert it into an electrical signal. The current response curve increases with joint bending and decreases with joint recovery. Each action can obtain a stable and repeatable response curve, and the response curve corresponding to a specific action is unique, which is determined by the joint structure and the particularity of the movement. It is worth noting that the deformation of different parts is different, and the relative current peak is also different. The differentiated sensing signals output by each sensor are sufficient to prove that the prepared sensor is sensitive enough to detect the subtle differences in human body movements. As shown in Fig. 5c and d, the strain sensor can accurately identify different angles of elbow and wrist bending. The relative current of the strain sensor increases during the deformation caused by the movement and decreases during the recovery of the deformation. The current peak also increases with the increase in the deformation angle of the joint movement. The elbow bending can cause a larger deformation than the wrist bending, resulting in a higher resistance value. Various body movements can be easily detected by the strain sensor and mapped to specific response curves, indicating that the prepared strain sensor can be applied to human posture correction and health warning. As shown in Fig. 5g, when the strain sensor is fixed at the knee joint, it can monitor the movement state and determine the real-time situations of slow walking, jogging and fast running, and output a unique and stable response curve. These results prove that the prepared strain sensor has high sensitivity and fast response characteristics, and as a flexible wearable electronic device, it can accurately detect the strain of human body movements and shows great application potential in the medical care field.

The human body's electrophysiological signals, as an important vital sign, are very common and routine in current clinical examinations since they contain a variety of health information about the human body. Thanks to its excellent flexibility and stretchability, the multi-layer structure pressure sensor can perfectly fit the irregular human skin and serve as a skin biosensor to detect the physiological electricity on the human epidermis. As shown in Fig. 5h, the pressure sensor can achieve continuous monitoring of the heartbeat, accurately perceive the weak pulse fluctuations of the human body, and detect the pulsation signals of the carotid artery and radial artery, *etc.* This is mainly attributed to its excellent mechanical properties, conductivity, and better adhesion and contact with the skin. Satisfactory results indicate that the pressure sensor can accurately detect and identify different action electromyographic signals, which means that its application in human–computer interaction and health assessment is feasible. Moreover, the sensor has good antibacterial and biocompatibility, which indicates that it has broader applicability and superior reliability in monitoring high-fidelity electrophysiological signals.

We compared the prepared multifunctional electronic skin with the electronic skins that have been reported in previous studies, as shown in Table S2. The comparison was made in terms of the preparation materials, preparation methods, whether they possess antibacterial and breathable properties, and the multifunctionality of the sensors. The electronic skin prepared in this work has obvious advantages in overall performance.

Conclusions

In summary, a multifunctional electronic skin was developed by integrating a modified Tecoflex electrospun nanofiber membrane (T-eNFM-3) with a multi-walled carbon nanotube (MWCNT)/silver (Ag powder) composite layer. The resulting device demonstrates outstanding breathability and antibacterial efficacy, ensuring user comfort and biocompatibility during extended wear. The micro-structured conductive layer was engineered by modulating the viscosity of the screen-printing ink. This enabled the design and fabrication of strain sensors (gauge factor, GF = 5.81) and multilayer pressure sensors (sensitivity, $S = 2.83\ \mathrm{kPa}^{-1}$), exhibiting response times of 50 ms and 280 ms, respectively. The strain sensor reliably monitors joint movements across the human body and effectively distinguishes locomotion states such as slow walking, jogging, and running. Concurrently, the pressure sensor enables detection of physiological signals including heartbeat, carotid pulse, and radial artery activity, offering comprehensive insight into cardiovascular function. This work presents a mechanically robust, flexible, and multifunctional platform that addresses limitations inherent to conventional electronic skin designs, with broad potential in wearable health monitoring, human–machine interfacing, and biomedical applications.

Author contributions

H. X. and E. H. conducted the experiments and collected the data. D. V. and T. H. contributed to data analysis and interpretation. K. H. assisted in manuscript revising. G. W. provided guidance on methodology and technical support. G. L. and Y. W. supervised the project and contributed to conceptual

development. J. J. coordinated the research activities, and drafted the manuscript. All authors reviewed and approved the final manuscript.

Conflicts of interest

The authors declare that they have no known competing financial interests or personal relationships that could have appeared to influence the work reported in this paper.

Data availability

All the relevant data of this study are available within the manuscript and its supplementary information (SI). Supplementary information is available. See DOI: **https://doi.org/10.1039/d5sc05696a**.

Acknowledgements

The authors would like to thank the following program for financial support: Beijing Natural Science Foundation (no. IS23045 to Y. W.).

References

1 H. Zhu, J. Wang, X. Yang, B. Zhang and Z. Wang, Tailoring Biopolymers for Electronic Skins: Materials Design and Applications, *Adv. Mater.*, 2025, **37**, 2413112.
2 Y. Chen, X. Zhang and C. Lu, Flexible piezoelectric materials and strain sensors for wearable electronics and artificial intelligence applications, *Chem. Sci.*, 2024, **15**, 16436–16466.
3 X. Fu, W. Cheng, G. Wan, Z. Yang and B. C. K. Tee, Toward an AI Era: Advances in Electronic Skins, *Chem. Rev.*, 2024, **124**, 9899–9948.
4 J. Ji, C. Cao, R. Qu, N. Zhou, E. He, M. Wu, H. Xiang, Z. Ma, G. Liu and Y. Wei, Flexible Waterborne Polyurethane-Bacterial Cellulose Films for Real-Time Physiological Monitoring, *Polymers*, 2025, **17**, 787.
5 H. Xiang, Z. Li, Z. Bai, H. Wu, G. Liu, H. Zhou and H. Liu, An E-skin for handwriting input at human-machine interface, *Chem. Eng. J.*, 2025, **505**, 158879.
6 Y. Li, W. Zhang, C. Zhao, W. Li, E. Dong, M. Xu, H. Huang, Y. Yang, L. Li, L. Zheng, M. Mao, S. Yao, L. Wang, J. Ma, X. Wang and W. Huang, Breaking the Saturation of Sensitivity for Ultrawide Range Flexible Pressure Sensors by Soft-Strain Effect, *Adv. Mater.*, 2024, **36**, 2405405.
7 R. Zhou, Y. Zhang, F. Xu, Z. Song, J. Huang, Z. Li, C. Gao, J. He, W. Gao and C. Pan, Hierarchical Synergistic Structure for High Resolution Strain Sensor with Wide Working Range, *Small*, 2023, **19**, 2301544.
8 M. Lei, K. Feng, S. Ding, M. Wang, Z. Dai, R. Liu, Y. Gao, Y. Zhou, Q. Xu and B. Zhou, Breathable and Waterproof Electronic Skin with Three-Dimensional Architecture for Pressure and Strain Sensing in Nonoverlapping Mode, *ACS Nano*, 2022, **16**, 12620–12634.
9 J. Chen, T. Song, X. Wang, Y. Zhou, T. Wang, X. Zhang, Y. Zhao, B. Yang, Y. Zhang, J. Chen, K. Chen, Y. Li and W. Han, Ultrasensitive and wide-range MXene/PDMS piezoresistive sensors inspired by rose petals, *Nano Energy*, 2024, **131**, 110285.
10 S. Zheng, W. Li, Y. Ren, Z. Liu, X. Zou, Y. Hu, J. Guo, Z. Sun and F. Yan, Moisture-Wicking, Breathable, and Intrinsically Antibacterial Electronic Skin Based on Dual-Gradient Poly(ionic liquid) Nanofiber Membranes, *Adv. Mater.*, 2022, **34**, 2106570.
11 H. Yang, S. Ji, I. Chaturvedi, H. Xia, T. Wang, G. Chen, L. Pan, C. Wan, D. Qi, Y.-S. Ong and X. Chen, Adhesive Biocomposite Electrodes on Sweaty Skin for Long-Term Continuous Electrophysiological Monitoring, *ACS Mater. Lett.*, 2020, **2**, 478–484.
12 J. Lv, G. Thangavel, Y. Li, J. Xiong, D. Gao, J. Ciou, M. W. M. Tan, I. Aziz, S. Chen, J. Chen, X. Zhou, W. C. Poh and P. S. Lee, Printable elastomeric electrodes with sweat-enhanced conductivity for wearables, *Sci. Adv.*, 2021, **7**, 8433.
13 M. Chao, L. He, M. Gong, N. Li, X. Li, L. Peng, F. Shi, L. Zhang and P. Wan, Breathable $Ti_3C_2T_x$ MXene/Protein Nanocomposites for Ultrasensitive Medical Pressure Sensor with Degradability in Solvents, *ACS Nano*, 2021, **15**, 9746–9758.
14 L. Teufel, A. Pipal, K. C. Schuster, T. Staudinger and B. Redl, Material-dependent growth of human skin bacteria on textiles investigated using challenge tests and DNA genotyping, *J. Appl. Microbiol*, 2010, **108**, 450–461.
15 G. Zhu, X. Wang, G. Zhang, Y. Yue, S. Yuan, H. Du, Z. Zhang, F. Ren, P. Ren and Q. Sun, Multifunctional Flexible Sensor with the Hybrid Staggered-Rib Conductive Network for Intelligent Recognition of Human Biomechanical and Electrophysiological Signals, *ACS Appl. Nano Mater.*, 2024, **7**, 24061–24070.
16 J. Dong, J. Hou, Y. Peng, Y. Zhang, H. Liu, J. Long, S. Park, T. Liu and Y. Huang, Breathable and Stretchable Epidermal Electronics for Health Management: Recent Advances and Challenges, *Adv. Mater.*, 2024, **36**, 2409071.
17 S. Wang, P. Fan, W. Liu, B. Hu, J. Guo, Z. Wang, S. Zhu, Y. Zhao, J. Fan, G. Li and L. Xu, Research Progress of Flexible Electronic Devices Based on Electrospun Nanofibers, *ACS Nano*, 2024, **18**, 31737–31772.
18 M.-M. Chen, S.-B. Cheng, K. Ji, J. Gao, Y.-L. Liu, W. Wen, X. Zhang, S. Wang and W.-H. Huang, Construction of a flexible electrochemiluminescence platform for sweat detection, *Chem. Sci.*, 2019, **10**, 6295–6303.
19 H. Hu, J. V. Buddingh, Z. Wang, B. Becher-Nienhaus and G. Liu, Patterning electrospun nanofiber mats for screen printing and other applications, *J. Mater. Chem. C*, 2018, **6**, 808–813.
20 X. Song, J. Ji, N. Zhou, M. Chen, R. Qu, H. Li, L. a. Zhang, S. Ma, Z. Ma and Y. Wei, Stretchable conductive fibers: design, properties and applications, *Prog. Mater. Sci.*, 2024, **144**, 101288.
21 Z. Ma, Q. Huang, Q. Xu, Q. Zhuang, X. Zhao, Y. Yang, H. Qiu, Z. Yang, C. Wang and Y. Chai, Permeable superelastic liquid-metal fibre mat enables biocompatible and monolithic stretchable electronics, *Nat. Mater.*, 2021, **20**, 859–868.

22 J. M. V. Makabenta, A. Nabawy, C.-H. Li, S. Schmidt-Malan, R. Patel and V. M. Rotello, Nanomaterial-based therapeutics for antibiotic-resistant bacterial infections, *Nat. Rev. Microbiol.*, 2021, **19**, 23–36.

23 S. Chen, Y. Xie, K. Ma, Z. Wei, X. Ran, X. Fu, C. Zhang and C. Zhao, Electrospun nanofibrous membranes meet antibacterial nanomaterials: From preparation strategies to biomedical applications, *Bioact. Mater.*, 2024, **42**, 478–518.

24 S. Shi, Y. Si, Y. Han, T. Wu, M. I. Iqbal, B. Fei, R. K. Li, J. Hu and J. Qu, Recent progress in protective membranes fabricated *via* electrospinning: advanced materials, biomimetic structures, and functional applications, *Adv. Mater.*, 2022, **34**, 2107938.

25 R. Du, X. Li, W. Wu, J. Zhou, Z. Liu, Y. Wang and T. Jiao, Black phosphorus-doped Janus structured electrospun fibrous membrane with antibacterial properties for wound healing, *Chem. Eng. J.*, 2025, **519**, 165605.

26 L. Tian, X. Zhu, L. Ma, J. Han, N. Yan, H. Zhang and W. Zhang, Waterproof and moisture-permeable electrospinning nanofiber membranes with high air permeability and mechanical properties using low-siloxane-modified waterborne polyurethane, *J. Environ. Chem. Eng.*, 2025, **13**, 115801.

27 G. A. Venegas-Cervera, A. I. Oliva, A. Avila-Ortega, J. M. Cervantes-Uc, L. M. Carrillo-Cocom and J. A. Juarez-Moreno, Biocompatibility studies of polyurethane electrospun membranes based on arginine as chain extender, *J Mater Sci-mater M*, 2021, **32**, 104.

28 Y. Yang, X. Li, Z. Zhou, Q. Qiu, W. Chen, J. Huang, W. Cai, X. Qin and Y. Lai, Ultrathin, ultralight dual-scale fibrous networks with high-infrared transmittance for high-performance, comfortable and sustainable PM0. 3 filter, *Nat. Commun.*, 2024, **15**, 1586.

29 J. Wang, J. Ye, Z. Li, X. Li, Y. Luo, Z. Zhou, C. Liu, T. Xu and X. Zhang, An Integrated Janus Bioelectronic Bandage for Unidirectional Pumping and Monitoring of Wound Exudate, *Nano Lett.*, 2025, **25**, 5156–5164.

30 J. Ji, N. Liu, Y. Tian, X. Li, H. Zhai, S. Zhao, Y. Liu, G. Liu, Y. Wei and L. Feng, Transparent polyurethane coating with synergistically enhanced antibacterial mechanism composed of low surface free energy and biocide, *Chem. Eng. J.*, 2022, **445**, 136716.

31 Y. Wang, R. Cao, C. Wang, X. Song, R. Wang, J. Liu, M. Zhang, J. Huang, T. You and Y. Zhang, In situ embedding hydrogen-bonded organic frameworks nanocrystals in electrospinning nanofibers for ultrastable broad-spectrum antibacterial activity, *Adv. Funct. Mater.*, 2023, **33**, 2214388.

32 Q. Li, X. Lai, Y. Duan, F. Jiang, Y. Li, Z. Huang, S. Liu, Y. Wang, C. Jiang and C. Zhang, 3D nanofiber sponge based on natural insect quaternized chitosan/pullulan/citric acid for accelerating wound healing, *Carbohydr. Polym.*, 2025, **348**, 122827.

33 Z. Jiang, W. Zhang, C. Zhu, Z. Hu, X. Xiang, D. Cao and X. Wang, Copper Telluride@Sodium Alginate-Poly(vinyl Alcohol) Nanofiber/Gauze Wound Dressing for Gram-Negative Bacteria-Infected Wounds, *ACS Nano*, 2025, **19**, 26170–26192.

34 X. Peng, K. Dong, C. Ye, Y. Jiang, S. Zhai, R. Cheng, D. Liu, X. Gao, J. Wang and Z. L. Wang, A breathable, biodegradable, antibacterial, and self-powered electronic skin based on all-nanofiber triboelectric nanogenerators, *Sci. Adv.*, 2020, **6**, eaba9624.

35 Y. Wang, L. Chu, S. Meng, M. Yang, Y. Yu, X. Deng, C. Qi, T. Kong and Z. Liu, Scalable and ultra-sensitive nanofibers coaxial yarn-woven triboelectric nanogenerator textile sensors for real-time gait analysis, *Adv. Sci.*, 2024, **11**, 2401436.

36 L. Yang, Y. Wu, B. Yang, H. Huang, H. He, S. Liu, C. Huang, Z. Qin, L. Zheng and C. Shen, Bioactive Nanoparticle-Embedded Micro/Nanofibrous Dressing with Improved Angiogenesis and Immunoregulation for Facilitating Burn Wound Healing, *Adv. Healthcare Mater.*, 2025, **14**, 2402886.